Volumetric energy density impact on mechanical properties of additively manufactured 718 Ni alloy

Benjamin Stegman[a], Anyu Shang[a], Luke Hoppenrath[a], Anant Raj[b], Hany Abdel-Khalik[b], John Sutherland[c], David Schick[d], and Victor Morgan[d], Kirti Jackson[d], Xinghang Zhang[a,] *,

[a] School of Materials Engineering, Purdue University, West Lafayette, IN 47907, USA

[b] School of Nuclear Engineering, Purdue University, West Lafayette, IN 47907, USA

[c] School of Environmental and Ecological Engineering, Purdue University, West Lafayette, IN 47907,

[d] Proto Precision Additive LLC, 4113 Leap Rd, Hilliard, OH 43026
*Corresponding author: X. Zhang, xzhang98@purdue.edu

Abstract

The 718 Ni-based superalloy has gained enormous attention in the additive manufacturing community for its great weldability, allowing for complex geometries to be formed, and its superb mechanical strength. Here we explore the influence of a wide range of major build parameters on microstructures and mechanical properties of 718 Ni alloys. Volumetric energy density appears to be one of the major parameters that capture the relationship between energy input and measured mechanical properties and microstructures of the alloys. A threshold energy density was identified below which the properties of the additively manufactured specimen degrade substantially. The influence of energy density on the quality of the built specimen simulated using Flow3D AM correlates well with the experimental results.

Keywords: nickel alloys, additive manufacturing, electron microscopy, mechanical properties, interfaces, energy density

1. Introduction

718 Ni-based superalloy fabricated by laser powder bed fusion (LPBF) has been extensively studied, partly because of its wide applicability to the aerospace and nuclear fields [1–3]. 718 Ni-based superalloy has a face centered cubic (FCC) γ matrix strengthened by γ' and γ" and has a maximum operating temperature of 650 °C [4,5]. In the as-printed (AP) state, the 718 Ni-based superalloy contains a columnar grain microstructure along the build (Z) direction and a more equiaxed morphology in the XY plane. Due to the high solidification speeds and thermal gradients, cells form with dislocations decorated around cell boundaries, unlike the typical dendritic casted equivalents [6,7]. This phenomenon leads to local solute rejection of heavy elements manifested by Nb and Mo microsegregation along the cell walls [8–11]. The dislocation cell walls act as diffusion pipelines for microsegregation [12]. During the LPBF process, residual heat leads to the precipitation of small scale laves and delta phase at the junctions of the cellular walls in the AP state [8,10,13]. The laves and delta phases are undesirable because they have limited slip systems, and lead to embrittlement [14–17].

With LPBF technology currently receiving such great attention, there is an industry-wide need for a parameter normalization technique to determine proper printing parameters that produce specific mechanical properties. The current best practice uses an empirical value called the volumetric energy density (VED) that is believed to be closely tied to process performance. The VED is defined as

$$VED = \frac{P}{v*h*d} \quad (1)$$

Where *P* is the amount of input energy, and *v*, *h* and *d* are the scanning speed, hatch spacing and layer thickness, respectively. Many researchers explored the effects of VED on the microstructure or mechanical properties of various alloys, and have noted that VED is a valuable evaluation tool [18,19,28–33,20–27].

Previous VED studies on alloy 718 and different materials have led the LPBF community to coin three printing regimes: lack of fusion (LOF), conduction, and keyholing regime [22,23,25–27,32–34]. LOF occurs when the chosen printing parameters input insufficient energy to overlap melt pools, thereby leaving pockets of partially sintered or unsintered powders. Porosity arising from LOF or trapped gases may drastically degrade mechanical properties, especially the fatigue life, of the material [35–39]. The conduction regime describes the parameter range where typical thermal conduction of the melt pool occurs and forms a typical semi-circular shape melt pool that is large enough to overlap with previous laser tracks to create a near fully dense material [22]. This regime is where the majority of parameter refinement occurs to optimize cell size, grain size, dislocation density and crystallographic orientation. The keyholing regime occurs at elevated VEDs, which causes the melt pool to become deep enough to trap many reflections of the laser beam [22,26], and a highly elongated melt pool generally forms. Subsequently porosity is trapped at the bottom of the pool because the melt pool folds back onto itself from extreme pressures of metal vaporization [29].

The microstructure, including grain size, cell size and crystallographic orientation is important in controlling mechanical properties. Watring et al. and Keshavarzkermani et al. show that a lower VED can decrease the matrix cell size as the thermal gradient increases and helps to further decrease the formation of laves phase by limiting the degree of solute rejection [23,30]. Cell size has been used as a microstructure parameter to describe Hall-Petch strengthening effect with some success [6,40,41]. The work by Voisin et al. and Riabov et al. supports this idea by identifying plastic deformation accumulation along the cellular walls using the Kernel average misorientation (KAM) maps generated from the electron beam scattering diffraction (EBSD) technique [7,42].

Grain structure in LPBF alloys is often characterized by the columnar grains in the ZY plane and smaller grains decorate the melt pool boundary while larger grains span across the melt pool width, in the XY plane [23,24]. Similar to cell size, grain size often increases with increasing VED [23,43,44]. The melt pool depth and width increase with the VED as the thermal gradient decreases, permitting greater degrees of continuous crystal growth. This enhanced crystal growth promotes specific crystallographic orientation. While depending on the underlying seed layer, the preferred crystallographic orientation should align with the direction of thermal gradient, which macroscopically is the build direction (BD), but locally is normal to the melt pool boundary [23,34]. For FCC metals, like the γ matrix, and body centered cubic (BCC) metals, the <100> crystallographic orientation typically solidifies along the orientation of the thermal gradient [45–47]. For various FCC systems such as 718 Ni-based superalloy, Hastelloy-X, 316 stainless steel and BCC systems such as pure chromium, once a high enough VED is reached, a preferred <100> texture aligns with the BD [19,20,24,33,48–50]. In contrast, a significant number of the LPBF studies reports a preferential <110> solidification direction aligned with the BD, once the VED has passed a certain threshold level [20,42,43,49,50]. More work is needed to unravel these discrepancies and identify the underlying causes. Nope et al. used the VED as a primary screening tool for porosity and microstructural optimization in 718 Ni-based superalloy [21]. The printing of three variants of a successful VED led to both successful and undesirable microstructures, suggesting the potential flaws behind this key parameter. In addition to VED, parameters such as laser spot size, build plate temperature and build strategy (i.e., layer rotation angle and/or island scanning) should be considered as they interplay into the outcoming microstructure and mechanical properties.

In the current study, we explore a wide range of printing parameters (including laser energy, scanning speed, hatching space, and laser spot size, and location within the build) on the evolution of microstructures and tensile properties of laser powder bed fused (LPBF) 718 Ni alloys. Our study suggests that VED can still be used a guiding parameter to tune the mechanical properties of the 718 alloys. Furthermore, a threshold VED has been identified below which the mechanical properties degrade substantially due to the defects induced by LOF.

2. Experimental Methods

718 Ni-based superalloy powders were purchased from Carpenter Inc. The powder lot was certified -16/+45μm and the respective chemistry can be found in Table 1.

	Ni	Cr	Fe	Nb+Ta	Mo	Ti	Al	Mn	Si	Co	C	Ta	O	N	B
IN718 (wt.%)	Bal.	19.23	18.79	4.99	3.00	0.98	0.45	0.02	0.04	0.06	0.03	0.05	0.02	0.01	<0.001

Table 1. Nominal measured powder chemistry of the IN 718 alloy.

Vertically aligned tensile bars with the dimensions of $50 \times 10 \times 1.5$ mm were printed with 5mm tall supports with a 45°-degree layer rotation build strategy in a Concept Laser M2 by Proto Precision Additive LLC. A combinatorial design of experiments, which combined laser powers of 300, 325 and 350W, scanning speeds of 750, 1000 and 1250 mm/s, and hatch spacings of 100, 130 and 160 μm, a layer thickness of 50μm and laser spot size of 150 μm were used to print 27 different parameter sets with 4 dogbones per set. These parameters, seen in Figure 1, were chosen to both create a systematic DOE as well as a widespread range of volumetric energy densities. The

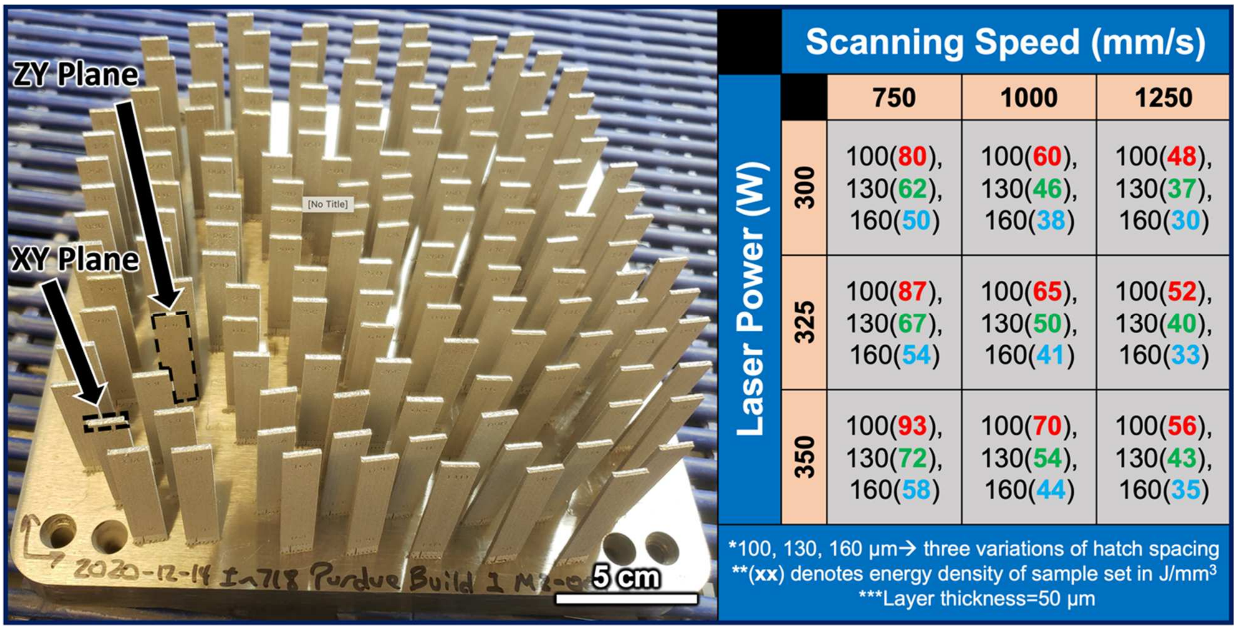

Figure 1. Macroscopic image of the build plate containing all vertical tension samples printed on support structures with each sample randomly distributed onto the build plate. Expeimental matrix showing three laser powers, 300-350 W, three scanning speeds, 750-1250 mm/s, and three different hatch spacings, 100-160 µm, with the volumetric energy densty bolded next to each hatch spacing. A 50 µm build layer thickness was used for the entire experiments. For reference the red, green and blue color coding of the VED represent the high, medium and low VEDs for each combination of laser power and scanning speed.

316 stainless steel build-plate was kept at 150 ºC and the oxygen concentration was maintained at or below 1500 ppm during the build process.

AP samples were prepared by standard mechanical grinding and polishing procedures to a sub-micron colloidal silica final step. X-ray diffraction (XRD) 2-theta peak analysis and residual stress measurements were conducted on a PANalytical Empyrean X'pert PRO MRD diffractometer with a 2 × Ge (220) hybrid monochromator to select Cu Kα1, using a step size of 0.3° and 0.005° and a time-per-step of 0.2 and 0.6 seconds, respectively. Due to sample geometry restrictions, XRD experiments were only conducted on the ZY plane to show texture and measure residual stress. The residual stress measurements followed the ASTM E112 standard, which focuses on a single planar XRD peak and measures it as chi (angle around x-axis) changes from 0°, 18.44°, 26.57°, 33.21°, 39.23° to 45°. The slight shift in peak 2Θ results in a change in interplanar spacing (D), which can be plotted versus the $\sin^2(\chi)$ producing a linear relationship. Then using equation 2, the residual stress can be calculated

$$\sigma_{residual} = \left(\frac{dD}{d\sin^2\chi}\right)\left(\frac{E}{1+\nu}\right)_{hkl}\left(\frac{1}{D_o}\right) \quad (2)$$

by measuring the slope of the change in interplanar spacing versus the change in $\sin^2\psi$ and using the elastic modulus (E) of that planar direction, the Poisson's ratio (ν) and the measured interplanar spacing at $\chi = 0$ (D_o) [51,52]. The chosen plane of interest was (111) and an average value of the E_{220} of 276 GPa and a Poisson's ratio of 0.29 were used for the calculation [53–56].

Scanning electron microscopy (SEM) micrographs were collected on a Thermo Fisher Quanta Field Emission Gun (FEG) 650 SEM. Secondary Electron (SE), Backscattered (BSE) and electron dispersive spectroscopy (EDS) SEM experiments were performed for fractography and microstructural analysis on a Quanta 650 SEM microscope equipped with an Ametek Hikari detector. An Ametek EDAX Hikari EBSD detector was utilized to quantify grain orientation, grain boundary characteristics and grain size distribution, using a step size of 0.8μm. Energy dispersive X-ray spectroscopy (EDS) experiments were used to characterize elemental segregation on a Quanta 3D FEG SEM.

All tension tests were carried out on an MTS machine, using a 30 kN load cell, an approximate 30 N preload to mitigate any slipping effects and a constant strain rate of 7.5×10^{-4} s^{-1}. Each tension sample was laser engraved from the tensile bars to a dogbone with the dimensions seen in Figure 4 and then mechanically ground and polished prior to testing. Work hardening rates were measured based on the modified power law work hardening,

$$\sigma_p = \sigma_0 + K\varepsilon^n \tag{3}$$

where σ_p, σ_0, K, ε and n are the plastic flow stress, yield stress (YS) value, strength coefficient, strain and the work hardening exponent, respectively [57]. Other work hardening models like ones proposed by Ludwigson and Tian-Zhang were assessed but the modified power law work hardening model was determined to be most applicable to the microstructures typical in LPBF alloy 718 and the observed work hardening behavior [58,59]. A modeled work hardening plot was then generated and the derivative of that was taken to model the work hardening rate. An instantaneous work hardening rate was also plotted and matched well with the modeled version. The intersection between the true stress-strain curve and either of these work hardening rates is the standard method for measuring the uniform elongation, or the onset of necking. This intersection point represents the onset of necking is also known as the Considère Criterion [60,61]. This method of determining the uniform elongation and ultimate tensile strength (UTS) was compared with simply taking the maximum stress value of the plastic region as the UTS and point of uniform elongation. This assumption matched well with the modeled values and therefore was used throughout this study due to its simplicity.

Flow3D AM is a commercial software package that contains a discrete element modeling (DEM) program to simulate powder settling simulations which then relies on a computational fluid dynamics (CFD) simulation that mimics a heat source (laser) and simulates the meso-scale melt pool thermal and internal velocity components. The settling simulations used a spring constant, coefficient of restitution (normal and tangential), particle & wall static friction coefficient, particle & wall dynamic static friction and cell size of 90, 0.3, 0.2, 0.15 and 56 µm, respectively. The powder size distribution (PSD) came from Microtrac data of a different lot of additive alloy 718 powder produced and measured by Praxair Surface Technologies Inc.. 10

different powder sizes were selected by averaging values of the upper and lower bins for each section and using their respective weight percentages. The settled layer was designed to be slightly thicker than the 50 µm layer used so that the layer thickness could be manually trimmed down to ~50µm. In the laser welding simulations, a 4-track simulation, each track length being ~600 µm in length, was run for all cases in the DOE matrix to evaluate the accuracy of the model and any insight it can provide for the experimental findings. The laser was given a circular shape with a gaussian powder distribution with a spot radius of 75 µm. The truncated 50 µm thick powder bed was placed onto a flat, fully dense 150 µm layer that was used to mimic a build plate. Both the powder bed and previous layer were preheated to 150 ºC to match the experimental settings. The multiple reflections mode was activated which assumed a Fresnel reflection mode and a maximum of 5 reflections to make the simulations more realistic.

3. Results

3.1 Mechanical properties, fracture surfaces and residual stress

Density, tensile strengths, and ductility results show clear and significant trends with respect to VED. Figure 2a-c show that the relative density, YS, and UTS increase prominently with increasing VED, until the VED reaches ~ 46 J/mm^3, beyond which the density slightly decreases, while the YS and UTS decrease moderately at a steady rate. As shown in Fig. 2d, the n value increases rapidly with VED up to ~ 46 J/mm^3, and then increases slightly afterwards.

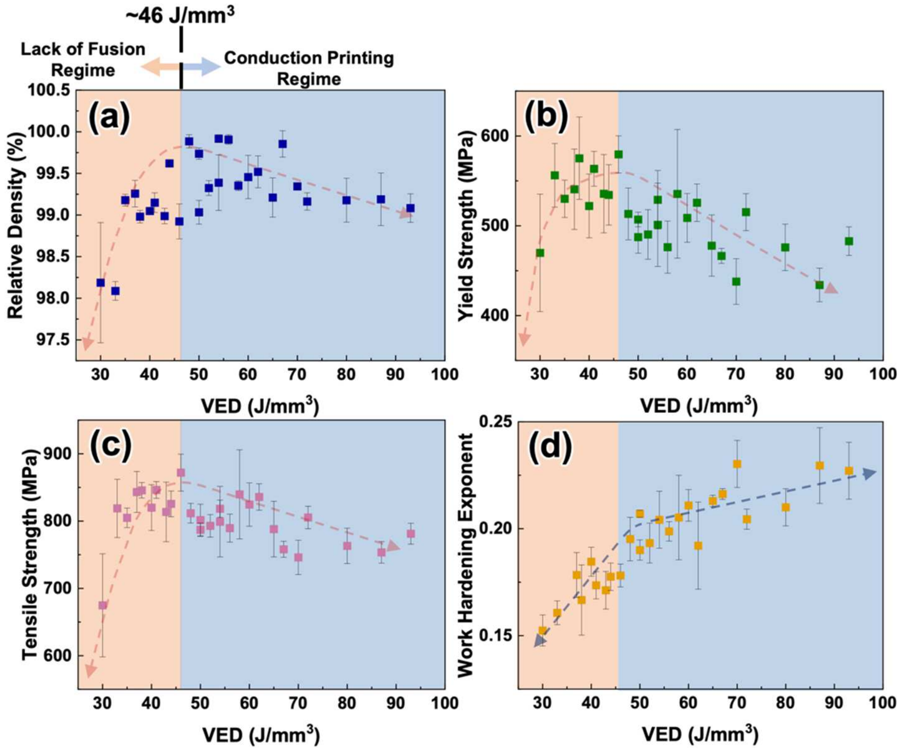

Figure 2. The variation of (a) relative density, (b) yield strength, (c) tensile strength, (d) work hardening exponent with volume energy density (VED).

Figure 3 (a) and (b) demonstrate how the uniform elongation and elongation to fracture behave similarly with an initial large increase with VED and then gradually increase beyond the VED of 46 J/mm^3. A prominent change in slope of all these plots occurs at the threshold value of ~46 J/mm^3. The YS/elongation-to-fracture ratio decays exponentially with respect to VED (Fig. 3(c)), meaning the point closest to origin would be the optimal parameters to have a well-balanced strength and formability. The parameters can be further tuned to an application's need of the material. Energy absorbed during plastic deformation (integration underneath the stress-strain curve) increases rapidly with VED, and reaches a plateau beyond 46 J/mm^3.

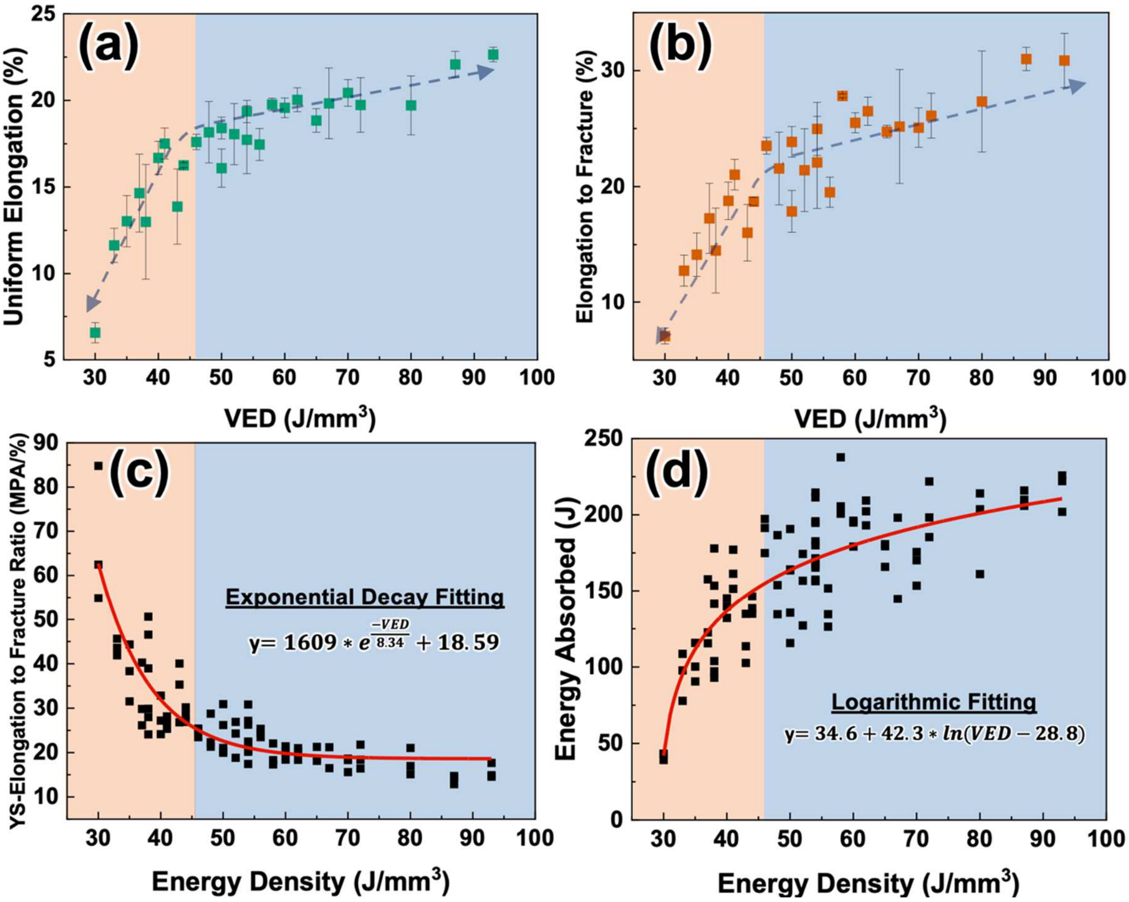

Figure 3. The influence of VED on (a) uniform elongation, (b) elongation to fracture, (c) the ratio of yield stress to elongation to fracture superimposed with an exponential decay fitting, and (d) absorbed energy superimposed with a logarithmic fitting line.

Among all specimens, sample sets with VED of 30, 46, and 93 J/mm^3 were chosen for comparisons because these VED parameters produced the specimens with quite different (lower and upper bound) mechanical properties. Figure 4 (a) shows that mechanical properties of each set of specimens are in general reproducible. For VED of 93 J/mm^3, the specimens had the best ductility (~ 30%). In contrast, samples with VED of 30 J/mm^3 had the lowest ductility (< 10%), and those printed at 46 J/mm^3 had the optimal strength and ductility. Furthermore, the YS of 46 J/mm^3 specimens is 580 ± 21 MPa, greater than the 93 J/mm^3 specimens, 483 ± 16 MPa. Figure

4 (b) shows that work hardening rate of 46 J/mm^3 and 93 J/mm^3 specimens is similar, whereas

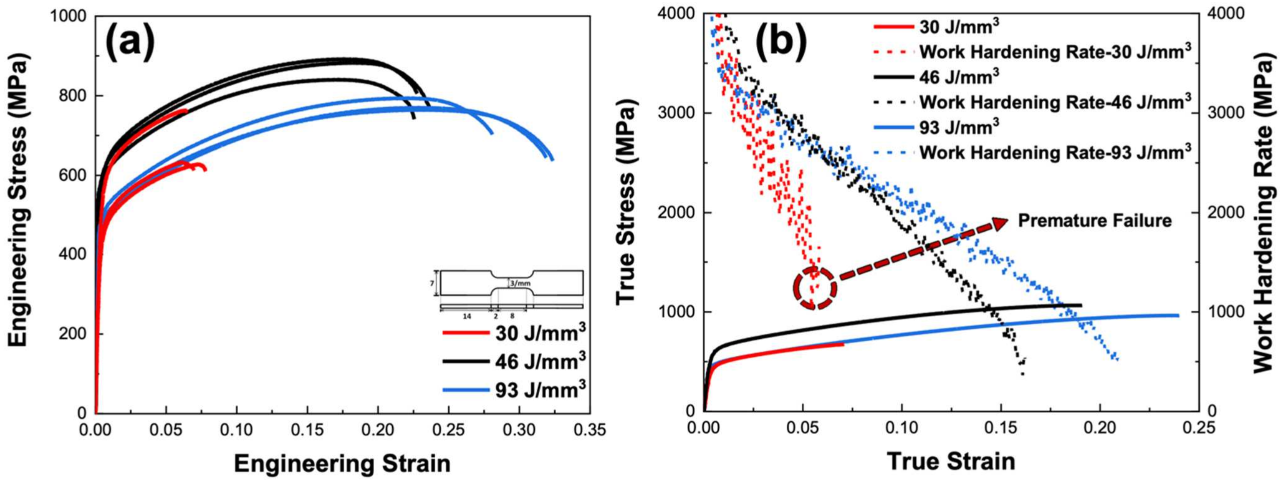

the work hardening rate of the 30 J/mm^3 is much less and does not intersect with the stress-strain plot.

Figure 4. (a) Comparison of engineering stress-strain curves for specimens manufactured using the three VEDs (30, 46, 93 J/mm^3). (b) Characteristic true stress-strain curves plotted with their respective work hardening rate.

Post deformation fractography revealed three different surface morphologies, faceted surface, inter-cellular fracture and ductile dimple fracture. Figure 5 (a), (d) and (g) show clear signs of residual powders due to lack of fusion (LOF) in the 30 J/mm^3 sample set. Figure 5 (b), (e), and (h) of the 46 J/mm^3 samples show small micro-cracks and cellular fracture surfaces. When VED = 93 J/mm^3, Figure 5 (c), (f) and (i) show the most ductile fracture surface manifested by high-density small dimples.

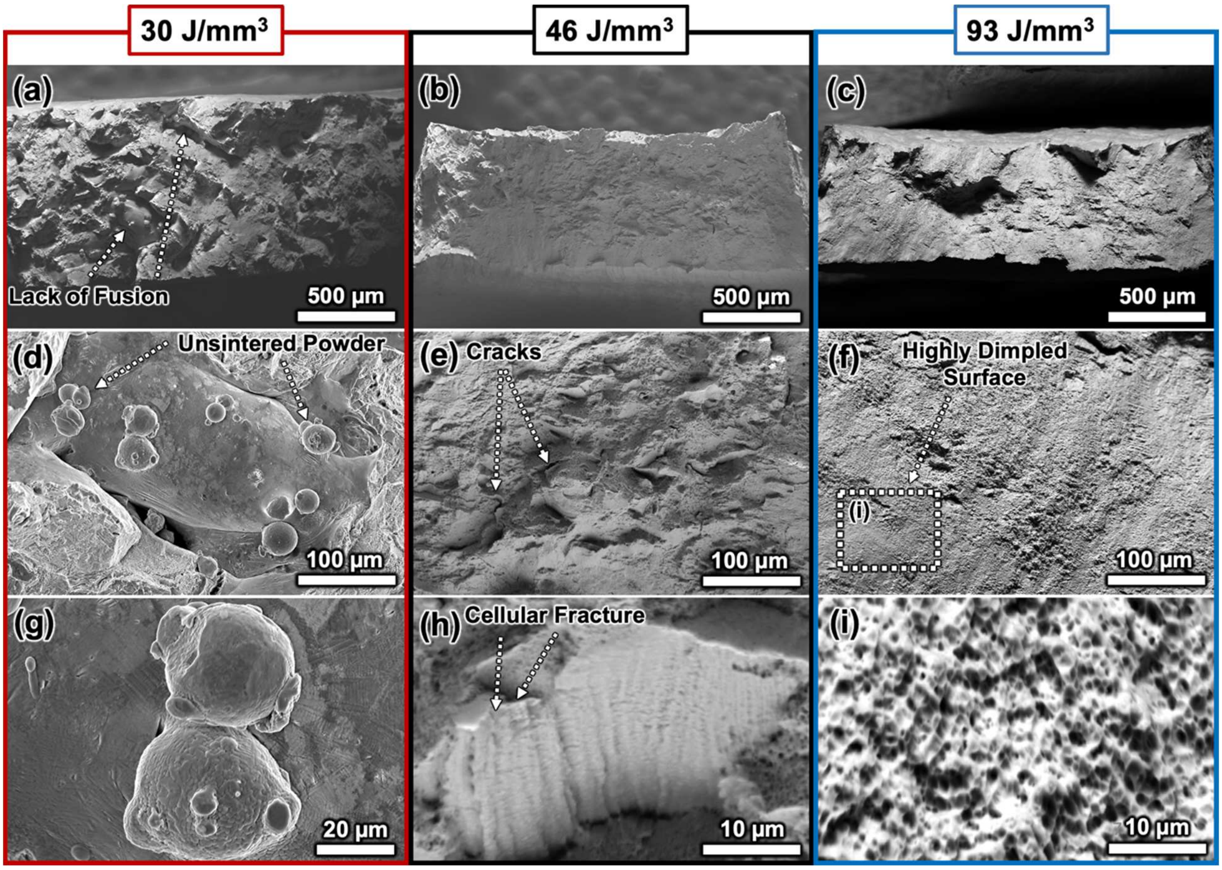

Figure 5. (a-c) Low magnification SEM micrographs of the fracture surfaces of the 30 J/mm^3, 46 J/mm^3 and 93 J/mm^3 samples, respectively. (d-f) Medium magnification SEM micrographs showing key differing features, such as unsintered powder in the 30 J/mm^3 specimen, cracks in 46 J/mm^3, and dimples in 93 J/mm^3 sample. (g-i) High magnification SEM micrographs revealing key features, the lack of fusion, inter-cellular and highly dimpled surface in each sample.

XRD experiments were conducted on all tested specimens on the ZY plane prior to tension testing. The 2-theta scans revealed that almost all parameter sets had a specific relative peak intensities. Figure 6 (a) shows that the (111) / (200) peak intensity ratio of 93 J/mm^3 specimens is similar to the alloy 718 powder. Whereas the (111) / (220) peak intensity ratio decreases rapidly with for VED of 30 J/mm^3, 46 J/mm^3. Residual stress measurements using the $\sin^2\chi$ method in Figure 6 (b) also revealed that 46 J/mm^3 specimen has the largest residual stress, followed by 93 J/mm^3 and then 30 J/mm^3 specimens.

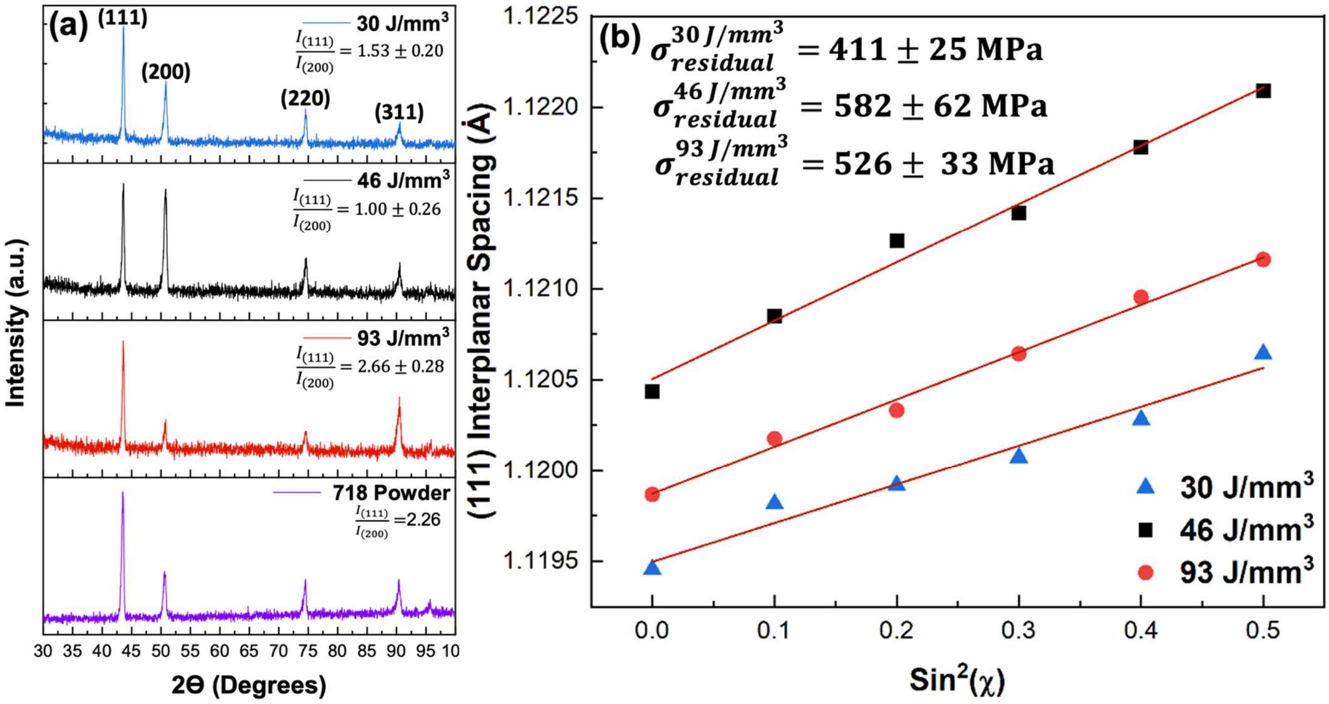

Figure 6. (a) Characteristic XRD spectra of the samples on ZY plane printed with different energy density and alloy 718 powder. (b) XRD (111)/(200) peak intensity ratio plotted vs. VED. (c) $\mathrm{Sin}^2\chi$ method used to determine the residual stress samples printed with various VED.

3.2 Microstructural Analysis

BSE SEM experiments were conducted to evaluate the microstructure of the as-printed specimens. The 30 J/mm^3 samples contained irregular shaped pores due to LOF. BSE SEM micrographs in Figure 7 (a) and (d) shows some examples of the pores near unsintered powder in both the XY and ZY planes. Dislocation cellular walls were decorated with precipitates and the average cell size is 1.94 µm. The 46 and 93 J/mm^3 samples have an average cell size of 1.39 and 2.95 µm (Fig. 7b-c). Precipitates were observed along cellular walls in both specimens. Columnar grain growth along cellular walls were also observed (Fig. 7e-f).

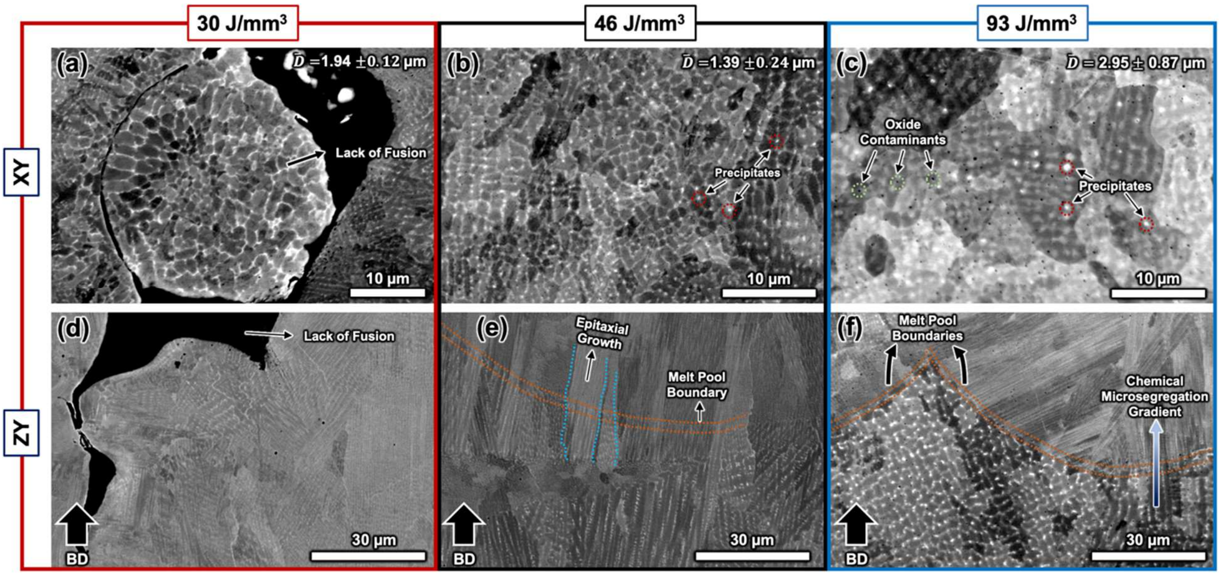

Figure 7. (a-c) Backscattered SEM micrographs of the XY plane, showing the polygonal cellular features of the 30 J/mm^3, 46 J/mm^3 and 93 J/mm^3 samples, respectively. Cell size (D) has been labeled in the figures. (d-f) Backscattered SEM micrographs of the ZY plane, highlighting the aligned columnar shape of the cells.

EDS experiments characterized the specific elements that segregate to the cell walls, Nb and Mo, with no other clear elemental segregation. Figure 8 shows the chemical segregation of Nb and Mo along the cellular walls in both the 46 and 93 J/mm^3 samples. Higher degrees of microsegregation were observed in the 46 J/mm^3 sample.

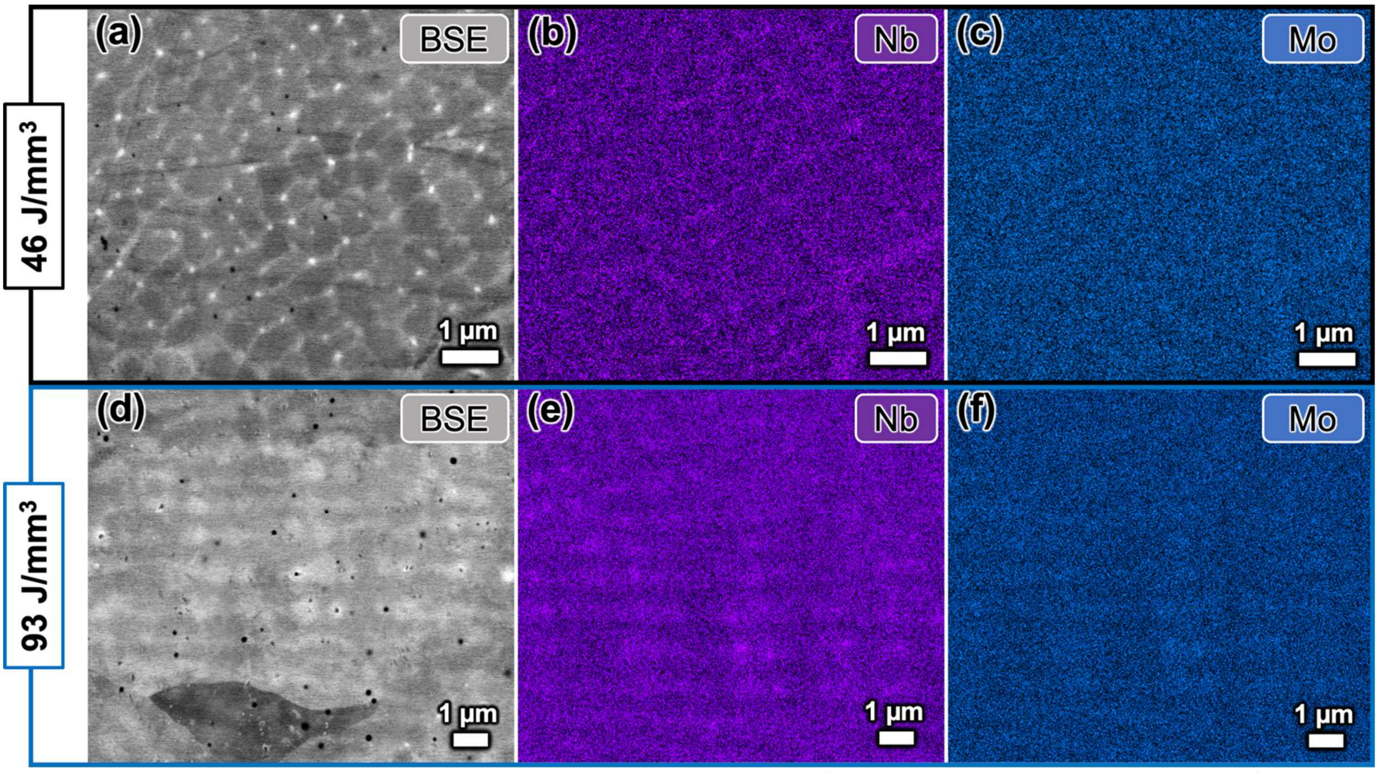

Figure 8. BSE and EDS micrographs of the 46 J/mm^3 samples (a-c) and the 93 J/mm^3 (d-f) samples, highlighting the Nb and Mo microsegregation along the cellular walls.

EBSD experiments were performed to examine the grain structure, grain boundary characteristics and crystallographic orientation in the undeformed state. The XY plane of the 30 J/mm^3 sample (Fig. 9a) shows an average respective grain width (W) and length (L) of 35 and 22 µm; and the ZY plan (Fig. 9d) shows columnar grains with W and L of 26 and 115 µm respectively. The 46 J/mm^3 specimen has an average W and L of 52 and 31 µm along XY plane (Fig. 9b), and an average columnar grain W and L of 29 and 175 µm on ZY plane (Fig. 9e).

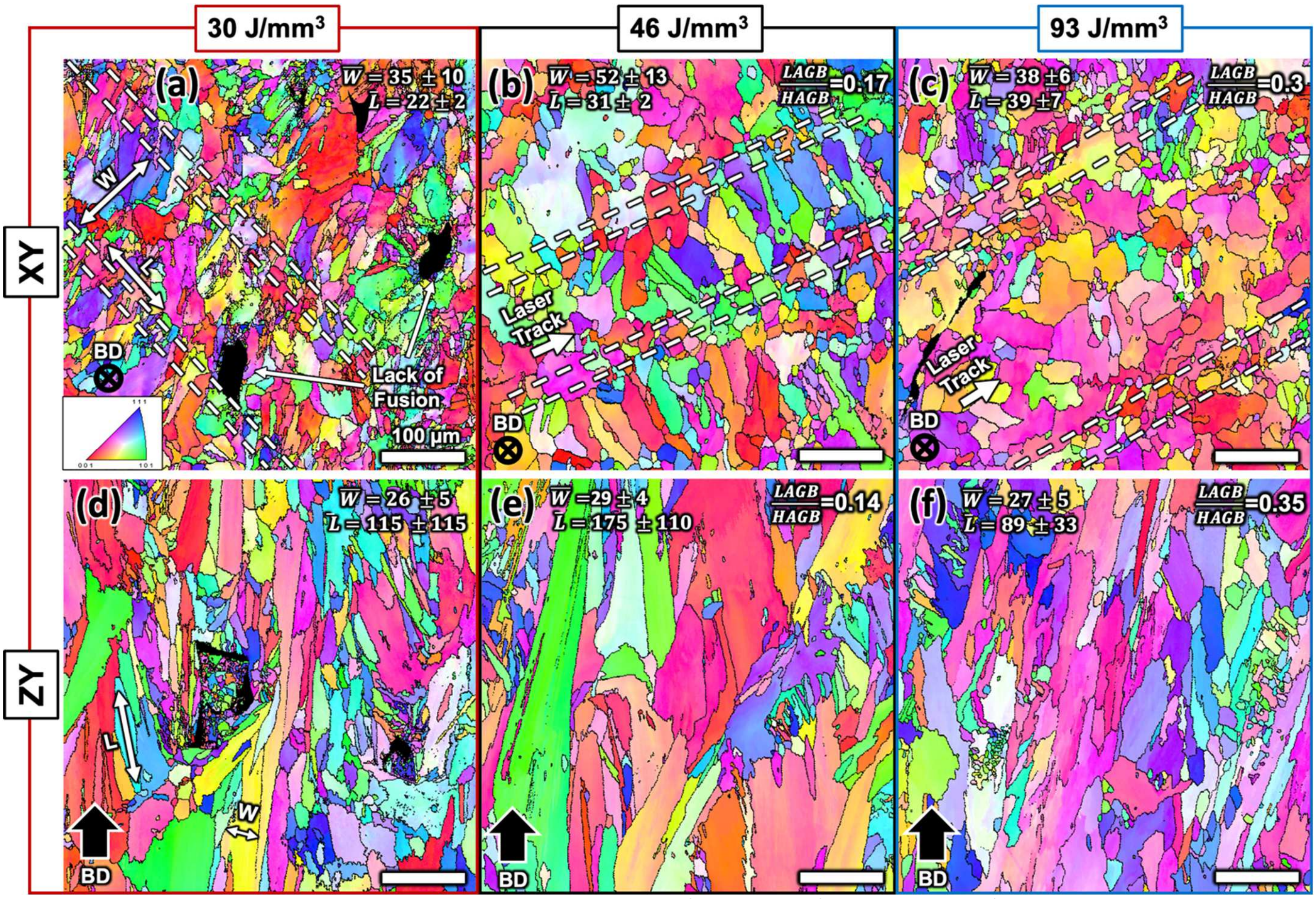

Figure 9. (a-c) IPFs of the XY plane of the 30 J/mm^3, 46 J/mm^3 and 93 J/mm^3 samples with respective grain width and length, and LAGB/HAGB ratios. (d-f) IPFs of the ZY plane for the corresponding specimens.

The 93 J/mm^3 sample sets have an average W and L of 38 and 39 µm on XY plane, and 27 and 89 µm on ZY plane. The ratio of low angle/high angle grain boundaries (LAGB/HAGB) is 14-17% for the 46 J/mm^3 specimen and 30-35% for the 93 J/mm^3 specimen. Also, there is no apparent preferred crystallographic orientation in the 30 and 46 J/mm^3 sample sets. But in the 93 J/mm^3 sample set, the XY plane shows a preference for <100> and <113> crystal orientation, while in the ZY plane, the preferred orientations appear to be <111> and <113>.

3.3 Flow3D Simulations

Figure 10 shows the XZ and YZ (side view) and XY (top-down view) perspectives of the three AM parameters sets of interest: 30 J/mm^3, 46 J/mm^3, 93 J/mm^3 used for Flow3D simulations (See supplementary video 1-3 for details). These simulations can be used to model the evolution of the melt pool depth, width and length for a given set of parameters. Additionally, the Computational fluid dynamics (CFD) modeling allows for the examination of LOF and porosity from keyholing. In this work, only LOF was observed in the 30 J/mm^3 sample set (Fig. 10 a,d,g) and the chosen VED ranges did not produce any form of keyholing defects, with the 93 J/mm^3 creating the widest and deepest melt pool.

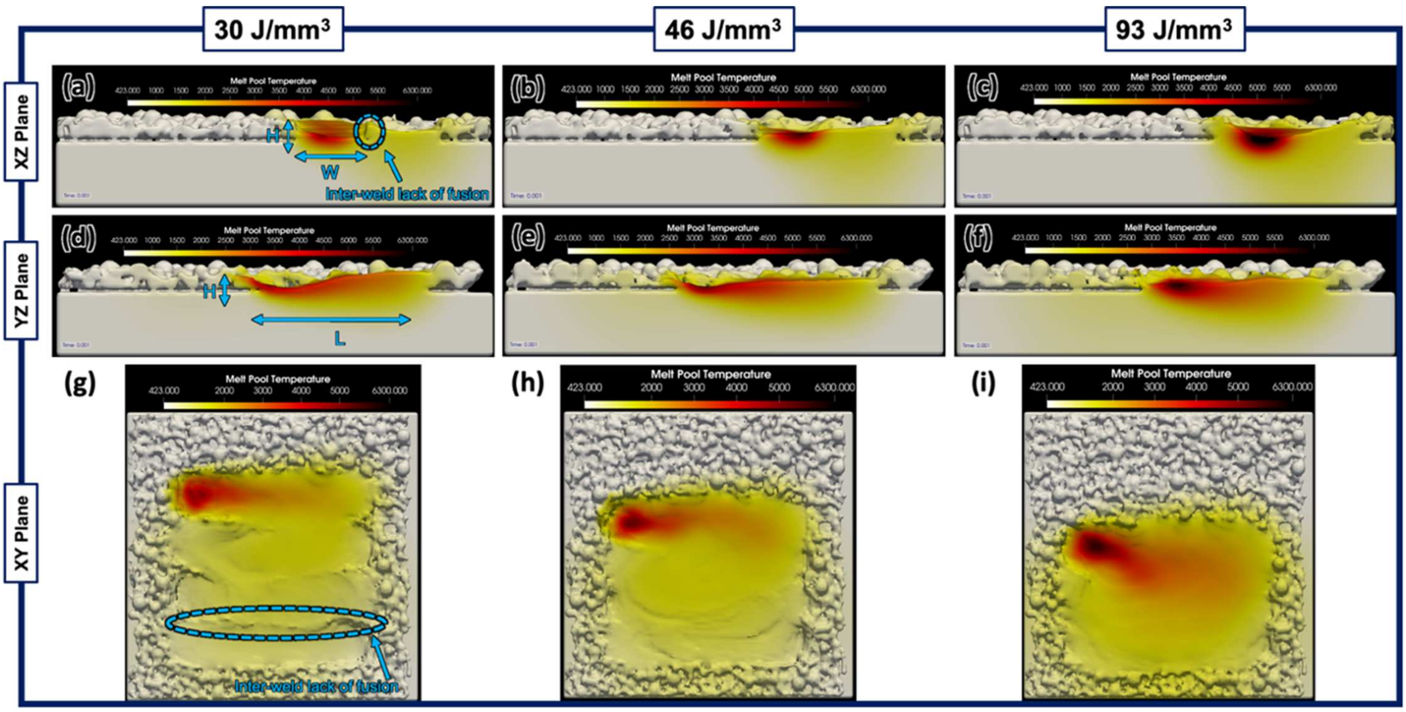

Figure 10. Flow3D snapshots of the 4 laser track simulations showing the (a-c) second track on the XZ plane of the 30 J/mm^3, 46 J/mm^3 and 93 J/mm^3 samples, (d-f) second track on the YZ plane of the corresponding samples, and (g-i) the full four track simulation on the XY planes of the 30 J/mm^3, 46 J/mm^3 and 93 J/mm^3 samples, respectively.

4. Discussion

4.1 Influence of VED on mechanical behavior

Fig. 2 and 3 reveal a threshold VED value, ~ 46 J/mm^3, where the density, YS and UTS reach a maximum. A similar trend has been observed by Wu et al. in AM AlSi10Mg [62]. They recorded an initial increase in mechanical strength until a threshold VED value where the typical trade-off between strength and ductility begins to take over, although their trends were less pronounced [25,62]. The AlSi10Mg showed signs of the keyholing regime as early as 50-70 J/mm^3, which was not seen in our 718 Ni-based superalloy. These difference can most likely be attributed to the large differences in melting temperature and powder-laser interaction due to aluminum's high reflectivity [63].

In this study, the largest YS difference, which was between the 46 J/mm^3 and 87 J/mm^3 sample sets, is ~100 MPa. The 30 J/mm^3 and 46 J/mm^3 sample sets exhibited the largest difference in UTS, 200 MPa. Varying laser energy density from 30 to 93 J/mm^3 led to reduction in work hardening exponent, uniform elongation and elongation to fracture by 33%, 16% and 24%, respectively. The large differences between the LOF and conduction regime is primarily caused by the porosity from LOF seen in Figure 5 (a), (d) and (g) and Figure 7 (a) and (d). These irregularly shaped pores have the most deleterious effects on the UTS, uniform elongation and elongation to fracture as shown in Figure 2 and Figure 3. Their differences in mechanical properties require a multifaceted explanation, including the grain boundary characteristics, cell size and residual stress.

4.2 Grain size, grain boundary nature and texture effect on mechanical behavior

The grain size marginally increases with increasing VED due to in-situ annealing and dislocation annihilation in the 93 J/mm^3 sample set during printing. But the overall strength differences between the 46 J/mm^3 and 93 J/mm^3 sample sets due to grain size difference in the XY or ZY plane is negligible. The morphology of the XY plane grains within the laser track shows a significant change. The 30 J/mm^3 sample contained smaller grain sizes in both the XY and ZY plane. The grains in the 46 J/mm^3 sample sets have the grains with typical higher aspect ratios spanning across the melt pool, while the 93 J/mm^3 sample sets have a more equiaxed grain structure within the laser tracks. The change in grain aspect ratio will likely affect the deformation behavior of the material. This morphological change is due to the melt pool becoming larger at higher VED, as modeled in Figure 10 (c) and 10 (f). The larger melt pools provide less geometrical constraints by reducing the steep thermal gradients normal to the melt pool.

Besides grain morphology changes, the nature of the GBs between these two sample sets is significantly different. The ratio of LAGB/HAGB in the 93 J/mm^3 sample set is 2 times as much as the 46 J/mm^3 sample. HAGBs are known to be stronger barriers than LAGBs to the transmission of dislocations, and hence increases the mechanical strength of metallic materials. Yalçinkaya et al. showed through a polycrystalline plasticity framework model that at a higher degrees of grain misorientations (i.e. HAGB) leads to a greater number of stress concentration points in a polycrystalline model [64]. This observation can partially explain the increased n observed in the 93 J/mm^3 sample set as shown in Figure 2(d) due to the increased ratio of LAGB/HAGB. Figure 9 also demonstrates a crystallographic shift in the XY and ZY plane from a random oriented grain structure in the 46 J/mm^3 specimen to a predominant <100> and <112> orientation. Prior studies show that for FCC metals, like the γ matrix, the <100>

crystallographic orientation typically solidifies along the orientation of the thermal gradient [45–47], and can become a predominant texture direction.

4.3 Cell size effect on mechanical behavior

Cellular morphology has been widely observed in LPBF materials. It has been argued that this unique microstructure provides increasing mechanical strength over its conventionally produced counterparts [6,65–72]. In this study, while the cell size and degree of microsegregation vary depending on relative location within each melt pool due to changing thermal gradients, certain trends can be identified. BSE studies show the area with the highest thermal gradients has the smallest cells with the least amount of microsegregation because solute rejection is suppressed. This phenomenon is apparent in Figure 7 (f), with the larger cells from the previous melt pool directly beneath the center of the melt pool boundary and the much finer cells growing upward from the melt pool boundary. The cell size is more irregular in the 30 J/mm^3 sample, likely due to enhanced nucleation around the LOF. Between the two fully dense sample sets (the 46 and 93 J/mm^3), an increase in cell size (D) by 100% from 1.39 to 2.95 μm was measured. The increase in cell size can be directly attributed to the decrease in thermal gradient caused by the larger melt pool of the higher VED sample sets [73]. The Flow3D simulations in Figure 10 prove that the 93 J/mm^3 sample displays the deepest and widest melt pool. Furthermore this increase in cell size has also been shown to correlate inversely with a decrease in YS, similar to the Hall-Petch relationship [68,69]. While using a similar Hall-Petch relationship has shown some success to describe in the increasing YS, a more comprehensive analysis is required in the future to accurately capture the cell size effect.

The variation in YS can be attributed partially to the solute segregation and density of dislocations along cell walls. The BSE micrographs in Figure 7 (b) and (e) clearly show dislocation cell wall contrast in the 46 J/mm^3 samples, and solute segregations along cell walls have been confirmed in EDS maps in Figure 8 (a-c). In contrast, in the 93 J/mm^3 samples, Figure 7 (c) show these enlarged cells have little to no cellular wall contrast. The lack of contrast implies the degree of microsegregation has been significantly reduced, as confirmed in Figure 8 (d-f). The reduced solute segregation and diminishing cell wall contrast indicate that the dislocation density along the cell walls in the 93 J/mm^3 samples is likely low and thus the resistance of these cell walls to the propagation of mobile dislocations may be low, leading to a reduced YS. Voisin et al. showed dislocation densities declined simultaneously with elemental homogenization during heat treatment [7]. The high VED in the 93 J/mm^3 specimen may have provided sufficient energy in the form of in-situ annealing for the previously solidified volumes around the laser, leading to reduced solute segregations, less dislocations along cell walls and a lower thermal gradient, which induces increased cell size.

Micropillar compressions presents an excellent technique to probe the effects of cells on mechanical behavior of AM alloys. Liu et al. has demonstrated with micropillar compression, that cell walls decorated with elemental segregation mainly provide strengthening without diminishing ductility [73]. Li et al. also discovered an increasing YS for smaller cell size in AM 316 stainless steel, and contended that the increasing dislocation density contributed to the increased YS [68]. This perspective agrees well with the increased strain accommodation along the dislocation cell walls shown by Voisin et al. [7].

4.4 Residual stress effect on mechanical behavior

The tensile residual stress, measured via the $\sin^2(\chi)$ method, in the 46 J/mm^3 samples is estimated to be 50 MPa greater than the 93 J/mm^3 samples. A greater tensile residual stress will lead to reduction of the measured YS and UTS as shown previously [74]. Hence it is likely that the 46 J/mm^3 sample may be intrinsically stronger than what we have measured experimentally if it does not have tensile residual stress. The influence of residual stress on mechanical behavior of AM 718 Ni alloys can be investigated by performing a series of heat treatment, which will be carried out in our future studies.

5. Conclusion

In this work, a detailed investigation of the relationship between VED and mechanical properties was conducted. The high density of data points span over a broad range of VED, 30-93 J/mm^3, making this study unique in reliably capturing the variation of mechanical properties with VED. The key finding is that VED can be used as a major parameter to describe the part quality in terms of their mechanical properties even though it may lack some ability to capture the full physics of the LPBF process. When decreasing VED from 93 to 46 J/mm^3, the YS and UTS increase accompanied by moderate reduction of work hardening exponent and uniform elongation, due to increasing fraction of high-angle grain boundaries and decreasing cell size, and the tensile residual stress slightly increases. Below 46 J/mm^3, the mechanical behavior of the alloy degrades substantially due to increasing LOF porosity. This study confirms the significance of VED in tailoring the microstructures and mechanical properties of LPBF 718 Ni alloys.

Acknowledgements

Stegman and Zhang would like to acknowledge the partial financial support from the DOE Nuclear Energy University Program (NEUP) under grant number DE-NE0008990. We acknowledge Proto Precision Additive LLC for providing the tensile coupons and their knowledgeable expertise in the field of LPBF. We also acknowledge access to the microscopy

center in the School of Materials Engineering and Life science microscopy facility at Purdue University.

Data availability

The raw/processed data required to reproduce these findings cannot be shared at this time due to technical or time limitations.

References

[1] C.L. English, S.K. Tewari, D.H. Abbott, An overview of ni base additive fabrication technologies for aerospace applications, 7th Int. Symp. Superalloy 718 Deriv. 2010. 1 (2010) 399–412. https://doi.org/10.1002/9781118495223.ch31.

[2] F. Klocke, C. Wagner, Direct Selective Laser Sintering of Superalloys 2 . Base test : sintering behaviour of 2 grains, Proc. Solid Free. Fabr. Symp. (2002) 187–198.

[3] R.M. Horn, M. Connor, D. Webber, J. Jackson, F. Bolger, Evaluation of additively manufactured materials for nuclear plant components, Miner. Met. Mater. Ser. (2019) 1009–1020. https://doi.org/10.1007/978-3-030-04639-2_63.

[4] R.E. Schafrik, D.D. Ward, J.R. Groh, Application of alloy 718 in GE aircraft engines: past, present and next five years, Proc. Int. Symp. Superalloys Var. Deriv. 1 (2001) 1–11. https://doi.org/10.7449/2001/superalloys_2001_1_11.

[5] C.F. Elefterie, C. Guragata, D. Bran, B. Ghiban, Aeronautical requirements for Inconel 718 alloy, IOP Conf. Ser. Mater. Sci. Eng. 209 (2017). https://doi.org/10.1088/1757-899X/209/1/012060.

[6] Y.M. Wang, T. Voisin, J.T. McKeown, J. Ye, N.P. Calta, Z. Li, Z. Zeng, Y. Zhang, W. Chen, T.T. Roehling, R.T. Ott, M.K. Santala, P.J. Depond, M.J. Matthews, A. V. Hamza, T. Zhu, Additively manufactured hierarchical stainless steels with high strength and ductility, Nat. Mater. 17 (2018) 63–70. https://doi.org/10.1038/NMAT5021.

[7] T. Voisin, J.B. Forien, A. Perron, S. Aubry, N. Bertin, A. Samanta, A. Baker, Y.M. Wang, New insights on cellular structures strengthening mechanisms and thermal stability of an austenitic stainless steel fabricated by laser powder-bed-fusion, Acta Mater. 203 (2021) 116476. https://doi.org/10.1016/j.actamat.2020.11.018.

[8] Y.L. Kuo, S. Horikawa, K. Kakehi, The effect of interdendritic δ phase on the mechanical properties of Alloy 718 built up by additive manufacturing, Mater. Des. 116 (2017) 411–418. https://doi.org/10.1016/j.matdes.2016.12.026.

[9] M. Ni, S. Liu, C. Chen, R. Li, X. Zhang, K. Zhou, Effect of heat treatment on the microstructural evolution of a precipitation-hardened superalloy produced by selective laser melting, Mater. Sci. Eng. A. 748 (2019) 275–285. https://doi.org/10.1016/j.msea.2019.01.109.

[10] H. Xiao, S.M. Li, W.J. Xiao, Y.Q. Li, L.M. Cha, J. Mazumder, L.J. Song, Effects of laser modes on Nb segregation and Laves phase formation during laser additive manufacturing of nickel-based superalloy, Mater. Lett. 188 (2017) 260–262. https://doi.org/10.1016/j.matlet.2016.10.118.

[11] E.L. Stevens, J. Toman, A.C. To, M. Chmielus, Variation of hardness, microstructure, and Laves phase distribution in direct laser deposited alloy 718 cuboids, Mater. Des. 119 (2017) 188–198. https://doi.org/10.1016/j.matdes.2017.01.031.

[12] M. Legros, G. Dehm, E. Arzt, T. John Balk, Observation of Giant Diffusivity Along Dislocation Cores, Science (80-.). 319 (2008) 1646–1649.

[13] H. Xiao, S. Li, X. Han, J. Mazumder, L. Song, Laves phase control of Inconel 718 alloy using quasi-continuous-wave laser additive manufacturing, Mater. Des. 122 (2017) 330–339. https://doi.org/10.1016/j.matdes.2017.03.004.

[14] S.G.K. Manikandan, D. Sivakumar, M. Kamaraj, Welding the Inconel 718 Superalloy, Weld. Inconel 718 Superalloy. (2019) 1–19. https://doi.org/10.1016/b978-0-12-818182-9.00001-3.

[15] M. Rafiei, H. Mirzadeh, M. Malekan, Micro-mechanisms and precipitation kinetics of delta (δ)phase in Inconel 718 superalloy during aging, J. Alloys Compd. 795 (2019) 207–212. https://doi.org/10.1016/j.jallcom.2019.05.001.
[16] X. Xie, J. Dong, G. Wang, W. You, J. Du, C. Zhao, Z. Wang, T. Carneiro, The effect of nb, ti, al on precipitation and strengthening behavior of 718 type superalloys, Proc. Int. Symp. Superalloys Var. Deriv. 3 (2005) 287–298. https://doi.org/10.7449/2005/superalloys_2005_287_298.
[17] H. Chandler, Heat treater's guide: practices and procedures for nonferrous alloys, 1996.
[18] F. Caiazzo, V. Alfieri, G. Casalino, On the Relevance of volumetric energy density in the investigation of inconel 718 laser powder bed fusion, Materials (Basel). 13 (2020). https://doi.org/10.3390/ma13030538.
[19] O. Gokcekaya, N. Hayashi, T. Ishimoto, K. Ueda, T. Narushima, T. Nakano, Crystallographic orientation control of pure chromium via laser powder bed fusion and improved high temperature oxidation resistance, Addit. Manuf. 36 (2020) 101624. https://doi.org/10.1016/j.addma.2020.101624.
[20] O. Gokcekaya, T. Ishimoto, S. Hibino, J. Yasutomi, Unique crystallographic texture formation in Inconel 718 by laser powder bed fusion and its effect on mechanical anisotropy, Acta Mater. 212 (2021) 116876. https://doi.org/10.1016/j.actamat.2021.116876.
[21] G. V. de Leon Nope, L.I. Perez-Andrade, J. Corona-Castuera, D.G. Espinosa-Arbelaez, J. Muñoz-Saldaña, J.M. Alvarado-Orozco, Study of volumetric energy density limitations on the IN718 mesostructure and microstructure in laser powder bed fusion process, J. Manuf. Process. 64 (2021) 1261–1272. https://doi.org/10.1016/j.jmapro.2021.02.043.
[22] Q. Chen, Y. Zhao, S. Strayer, Y. Zhao, K. Aoyagi, Y. Koizumi, A. Chiba, W. Xiong, A.C. To, Elucidating the effect of preheating temperature on melt pool morphology variation in Inconel 718 laser powder bed fusion via simulation and experiment, Addit. Manuf. 37 (2021) 101642. https://doi.org/10.1016/j.addma.2020.101642.
[23] D.S. Watring, J.T. Benzing, N. Hrabe, A.D. Spear, Effects of laser-energy density and build orientation on the structure–property relationships in as-built Inconel 718 manufactured by laser powder bed fusion, Addit. Manuf. 36 (2020) 101425. https://doi.org/10.1016/j.addma.2020.101425.
[24] Y. Tsutsumi, T. Ishimoto, T. Oishi, T. Manaka, P. Chen, M. Ashida, K. Doi, H. Katayama, T. Hanawa, T. Nakano, Crystallographic texture- and grain boundary density-independent improvement of corrosion resistance in austenitic 316L stainless steel fabricated via laser powder bed fusion, Addit. Manuf. 45 (2021) 102066. https://doi.org/10.1016/j.addma.2021.102066.
[25] H. Wu, Y. Ren, J. Ren, L. Liang, R. Li, Q. Fang, A. Cai, Q. Shan, Y. Tian, I. Baker, Selective laser melted AlSi10Mg alloy under melting mode transition_ Microstructure evolution, nanomechanical behaviors and tensile properties, J. Alloys Compd. 873 (2021) 159823. https://doi.org/10.1016/j.jallcom.2021.159823.
[26] L. Scime, J. Beuth, Melt pool geometry and morphology variability for the Inconel 718 alloy in a laser powder bed fusion additive manufacturing process, Addit. Manuf. 29 (2019) 100830. https://doi.org/10.1016/j.addma.2019.100830.
[27] A. Hilaire, E. Andrieu, X. Wu, High-temperature mechanical properties of alloy 718 produced by laser powder bed fusion with different processing parameters, Addit. Manuf. 26 (2019) 147–160. https://doi.org/10.1016/j.addma.2019.01.012.

[28] C.M. Cepeda-Jiménez, F. Potenza, E. Magalini, V. Luchin, A. Molinari, M.T. Pérez-Prado, Effect of energy density on the microstructure and texture evolution of Ti-6Al-4V manufactured by laser powder bed fusion, Mater. Charact. 163 (2020) 110238. https://doi.org/10.1016/j.matchar.2020.110238.
[29] S. Shrestha, Y. Kevin Chou, A Numerical Study on the Keyhole Formation During Laser Powder Bed Fusion Process, J. Manuf. Sci. Eng. 141 (2019) 1–9. https://doi.org/10.1115/1.4044100.
[30] A. Keshavarzkermani, E. Marzbanrad, R. Esmaeilizadeh, Y. Mahmoodkhani, U. Ali, P.D. Enrique, N.Y. Zhou, A. Bonakdar, E. Toyserkani, An investigation into the effect of process parameters on melt pool geometry, cell spacing, and grain refinement during laser powder bed fusion, Opt. Laser Technol. 116 (2019) 83–91. https://doi.org/10.1016/j.optlastec.2019.03.012.
[31] S. Shrestha, K. Chou, A study of transient and steady-state regions from single-track deposition in laser powder bed fusion, J. Manuf. Process. 61 (2021) 226–235. https://doi.org/10.1016/j.jmapro.2020.11.023.
[32] P. kumar, J. Farah, Influence of laser processing parameters on porosity in Inconel 718 during additive manufacturing, Mater. Lett. 252 (2019) 256–259. https://doi.org/10.1016/j.matlet.2019.05.114.
[33] H. Choo, K.L. Sham, J. Bohling, A. Ngo, X. Xiao, Y. Ren, P.J. Depond, M.J. Matthews, E. Garlea, Effect of laser power on defect, texture, and microstructure of a laser powder bed fusion processed 316L stainless steel, Mater. Des. 164 (2019) 107534. https://doi.org/10.1016/j.matdes.2018.12.006.
[34] J.G. Pauza, W.A. Tayon, A.D. Rollett, Computer simulation of microstructure development in powder-bed additive manufacturing with crystallographic texture Computer simulation of microstructure development in powder-bed additive manufacturing with crystallographic, (2021). https://doi.org/10.1088/1361-651X/ac03a6.
[35] A. Kaletsch, S. Qin, S. Herzog, C. Broeckmann, Influence of high initial porosity introduced by laser powder bed fusion on the fatigue strength of Inconel 718 after post-processing with hot isostatic pressing, Addit. Manuf. 47 (2021) 102331. https://doi.org/10.1016/j.addma.2021.102331.
[36] P. Edwards, M. Ramulu, Fatigue performance evaluation of selective laser melted Ti-6Al-4V, Mater. Sci. Eng. A. 598 (2014) 327–337. https://doi.org/10.1016/j.msea.2014.01.041.
[37] G. Kasperovich, J. Hausmann, Improvement of fatigue resistance and ductility of TiAl6V4 processed by selective laser melting, J. Mater. Process. Technol. 220 (2015) 202–214. https://doi.org/10.1016/j.jmatprotec.2015.01.025.
[38] L. Du, G. Qian, L. Zheng, Y. Hong, Influence of processing parameters of selective laser melting on high-cycle and very-high-cycle fatigue behaviour of Ti-6Al-4V, Fatigue Fract. Eng. Mater. Struct. 44 (2021) 240–256. https://doi.org/10.1111/ffe.13361.
[39] L. Sheridan, J.E. Gockel, O.E. Scott-Emuakpor, Stress-defect-life interactions of fatigued additively manufactured alloy 718, Int. J. Fatigue. 143 (2021) 106033. https://doi.org/10.1016/j.ijfatigue.2020.106033.
[40] D. Wang, C. Song, Y. Yang, Y. Bai, Investigation of crystal growth mechanism during selective laser melting and mechanical property characterization of 316L stainless steel parts, Mater. Des. 100 (2016) 291–299. https://doi.org/10.1016/j.matdes.2016.03.111.
[41] Y. Zhong, L. Liu, S. Wikman, D. Cui, Z. Shen, Intragranular cellular segregation network structure strengthening 316L stainless steel prepared by selective laser melting, J. Nucl.

Mater. 470 (2016) 170–178. https://doi.org/10.1016/j.jnucmat.2015.12.034.
[42] D. Riabov, A. Leicht, J. Ahlström, E. Hryha, Investigation of the strengthening mechanism in 316L stainless steel produced with laser powder bed fusion, Mater. Sci. Eng. A. 822 (2021). https://doi.org/10.1016/j.msea.2021.141699.
[43] A. Leicht, M. Rashidi, U. Klement, E. Hryha, Effect of process parameters on the microstructure, tensile strength and productivity of 316L parts produced by laser powder bed fusion, Mater. Charact. 159 (2020) 110016. https://doi.org/10.1016/j.matchar.2019.110016.
[44] M. Letenneur, A. Kreitcberg, V. Brailovski, The average grain size and grain aspect ratio in metal laser powder bed fusion: Modeling and experiment, J. Manuf. Mater. Process. 4 (2020). https://doi.org/10.3390/jmmp4010025.
[45] D.Y. Li, J.A. Szpunar, Texture competition in solidification process, Mater. Sci. Forum. 157–6 (1994) 547–554. https://doi.org/10.4028/www.scientific.net/msf.157-162.547.
[46] R.F. Mehl, Solidification of Metals and ALloys, AIME. (1951).
[47] T. Matching, R. Test, SOLIDIFICATION, Test. 1937 (1996) 162–173. https://doi.org/10.1016/B978-0-444-89875-3.50013-2.
[48] G.E. Bean, T.D. McLouth, D.B. Witkin, S.D. Sitzman, P.M. Adams, R.J. Zaldivar, Build Orientation Effects on Texture and Mechanical Properties of Selective Laser Melting Inconel 718, J. Mater. Eng. Perform. 28 (2019) 1942–1949. https://doi.org/10.1007/s11665-019-03980-w.
[49] S.H. Sun, T. Ishimoto, K. Hagihara, Y. Tsutsumi, T. Hanawa, T. Nakano, Excellent mechanical and corrosion properties of austenitic stainless steel with a unique crystallographic lamellar microstructure via selective laser melting, Scr. Mater. 159 (2019) 89–93. https://doi.org/10.1016/j.scriptamat.2018.09.017.
[50] S. Hibino, T. Todo, T. Ishimoto, O. Gokcekaya, Y. Koizumi, K. Igashira, T. Nakano, Control of crystallographic texture and mechanical properties of hastelloy-X via laser powder bed fusion, Crystals. 11 (2021) 1–12. https://doi.org/10.3390/cryst11091064.
[51] P.S. Prevéy, X-Ray Diffraction Characterization of Residual Stresses Produced By Shot Peening, Shot Peen. Theory Appl. c (1990) 81–93.
[52] A. Thesis, O. Anderoglu, Residual Stress Measurement Using X-Ray Diffraction Residual Stress Measurement Using X-Ray Diffraction, (2004).
[53] G. Martin, N. Ochoa, K. Saï, E. Hervé-Luanco, G. Cailletaud, A multiscale model for the elastoviscoplastic behavior of Directionally Solidified alloys: Application to FE structural computations, Int. J. Solids Struct. 51 (2014) 1175–1187. https://doi.org/10.1016/j.ijsolstr.2013.12.013.
[54] P. Haldipur, Estimation of Single-Crystal Elastic Constants from Ultrasonic Measurements on Polycrystalline Specimens, 1061 (2004) 1061–1068. https://doi.org/10.1063/1.1711735.
[55] S. Jothi, S. V. Merzlikin, T.N. Croft, J. Andersson, S.G.R. Brown, An investigation of micro-mechanisms in hydrogen induced cracking in nickel-based superalloy 718, J. Alloys Compd. 664 (2016) 664–681. https://doi.org/10.1016/j.jallcom.2016.01.033.
[56] Inconel, INCONEL alloy 718, Spec. Met. (2014) 1–27.
[57] W. Ramberg, W.R. Osgood, Description of stress-strain curves by three parameters, Natl. Advis. Comm. Aeronaut. (1943) Technical Note No. 902. http://hdl.handle.net/2060/19930081614.
[58] D.C. Ludwigson, U.S. Steel, Modified Stress-Strain Relation for FCC Metals and Alloys,

2 (1971) 2825–2828.
[59] X. Tian, Y. Zhang, Mathematical description for flow curves of some stable austenitic steels, 174 (1994) 7–9.
[60] Z.S. Basinski, M.S. Szczerba, J.D. Embury, Tensile instability in face-centred cubic materials, Philos. Mag. A Phys. Condens. Matter, Struct. Defects Mech. Prop. 76 (1997) 743–752. https://doi.org/10.1080/01418619708214207.
[61] J.J. Jonas, R.A. Holt, C.E. Coleman, Plastic stability in tension and compression, Acta Metall. 24 (1976) 911–918. https://doi.org/10.1016/0001-6160(76)90039-0.
[62] H. Wu, J. Ren, Q. Huang, X. Zai, L. Liu, C. Chen, S. Liu, X. Yang, R. Li, Effect of laser parameters on microstructure, metallurgical defects and property of alsi10mg printed by selective laser melting, J. Micromechanics Mol. Phys. 2 (2017) 1–15. https://doi.org/10.1142/S2424913017500175.
[63] S. Patel, H. Chen, M. Vlasea, Y. Zou, The influence of divergent laser beams on the laser powder bed fusion of a high reflectivity aluminium alloy, ArXiv. (2021) 1–25.
[64] T. Yalçinkaya, İ. Özdemir, İ. Tarik Tandoğan, Misorientation and grain boundary orientation dependent grain boundary response in polycrystalline plasticity, Comput. Mech. 67 (2021) 937–954. https://doi.org/10.1007/s00466-021-01972-z.
[65] Y. Li, A.J. Bushby, D.J. Dunstan, The Hall-Petch effect as a manifestation of the general size effect, Proc. R. Soc. A Math. Phys. Eng. Sci. 472 (2016). https://doi.org/10.1098/rspa.2015.0890.
[66] Y. Wang, Y. ting Wang, R. di Li, P. da Niu, M. bo Wang, T. chui Yuan, K. Li, Hall-Petch relationship in selective laser melting additively manufactured metals: using grain or cell size?, J. Cent. South Univ. 28 (2021) 1043–1057. https://doi.org/10.1007/s11771-021-4678-x.
[67] T.G. Gallmeyer, S. Moorthy, B.B. Kappes, M.J. Mills, B. Amin-Ahmadi, A.P. Stebner, Knowledge of process-structure-property relationships to engineer better heat treatments for laser powder bed fusion additive manufactured Inconel 718, Addit. Manuf. 31 (2020) 100977. https://doi.org/10.1016/j.addma.2019.100977.
[68] Z. Li, B. He, Q. Guo, Strengthening and hardening mechanisms of additively manufactured stainless steels: The role of cell sizes, Scr. Mater. 177 (2020) 17–21. https://doi.org/10.1016/j.scriptamat.2019.10.005.
[69] E. Hug, M. Lelièvre, C. Folton, A. Ribet, M. Martinez-Celis, C. Keller, Additive manufacturing of a Ni-20 wt%Cr binary alloy by laser powder bed fusion: Impact of the microstructure on the mechanical properties, Mater. Sci. Eng. A. 834 (2022). https://doi.org/10.1016/j.msea.2022.142625.
[70] N. Yang, J. Yee, B. Zheng, K. Gaiser, T. Reynolds, L. Clemon, W.Y. Lu, J.M. Schoenung, E.J. Lavernia, Process-Structure-Property Relationships for 316L Stainless Steel Fabricated by Additive Manufacturing and Its Implication for Component Engineering, J. Therm. Spray Technol. 26 (2017) 610–626. https://doi.org/10.1007/s11666-016-0480-y.
[71] F. Weng, Y. Chew, Z. Zhu, X. Yao, L. Wang, F.L. Ng, S. Liu, G. Bi, Excellent combination of strength and ductility of CoCrNi medium entropy alloy fabricated by laser aided additive manufacturing, Addit. Manuf. 34 (2020) 101202. https://doi.org/10.1016/j.addma.2020.101202.
[72] P. Krakhmalev, G. Fredriksson, K. Svensson, I. Yadroitsev, I. Yadroitsava, M. Thuvander, R. Peng, Microstructure, solidification texture, and thermal stability of 316 L stainless

steel manufactured by laser powder bed fusion, Metals (Basel). 8 (2018). https://doi.org/10.3390/met8080643.
[73] L. Liu, Q. Ding, Y. Zhong, J. Zou, J. Wu, Y.L. Chiu, J. Li, Z. Zhang, Q. Yu, Z. Shen, Dislocation network in additive manufactured steel breaks strength–ductility trade-off, Mater. Today. 21 (2018) 354–361. https://doi.org/10.1016/j.mattod.2017.11.004.
[74] B. Yang, Z. Shang, J. Ding, J. Lopez, W. Jarosinski, T. Sun, N. Richter, Y. Zhang, H. Wang, X. Zhang, Acta Materialia Investigation of strengthening mechanisms in an additively manufactured Haynes 230 alloy, 222 (2022). https://doi.org/10.1016/j.actamat.2021.117404.